CHALMERS
UNIVERSITY OF TECHNOLOGY

Focused Ion Beam induced hydride formation does not affect Fe, Ni, Cr-clusters in irradiated Zircaloy-2

Citation for the original published paper (version of record):
Mayweg, D., Eriksson, J., Bäcke, O. et al (2023). Focused Ion Beam induced hydride formation does not affect Fe, Ni, Cr-clusters in irradiated
Zircaloy-2. Journal of Nuclear Materials, 581. http://dx.doi.org/10.1016/j.jnucmat.2023.154444

Journal of Nuclear Materials 581 (2023) 154444

Contents lists available at ScienceDirect

Journal of Nuclear Materials

journal homepage: www.elsevier.com/locate/jnucmat

Focused Ion Beam induced hydride formation does not affect Fe, Ni, Cr-clusters in irradiated Zircaloy-2

David Mayweg[a,*], Johan Eriksson[a], Olof Bäcke[a], Andrew J. Breen[b,c], Mattias Thuvander[a]

[a] Department of Physics, Chalmers University of Technology, SE-412 96 Gothenburg, Sweden
[b] School of Aerospace, Mechanical & Mechatronic Engineering, The University of Sydney, Sydney, NSW, Australia
[c] Australian Centre for Microscopy & Microanalysis, The University of Sydney, Sydney, NSW, Australia

ARTICLE INFO

Article history:
Received 8 September 2022
Revised 6 April 2023
Accepted 11 April 2023
Available online 11 April 2023

Keywords:
Atom probe tomography
Zirconium hydrides
Zirconium fuel cladding
Clustering
Irradiation effects
Focused ion beam

ABSTRACT

Room temperature focused ion beam (FIB) milling is known to potentially promote the formation of hydrides in zirconium and its alloys. We used atom probe tomography (APT) to determine the composition of irradiated and as-produced Zircaloy-2 fuel cladding. We consistently found ∼ 50 at% hydrogen in all room temperature FIB-milled specimens run in voltage pulsing APT measurements. Crystallographic analysis of APT data however showed slightly better agreement with δ-hydride (ZrH_2, FCC, ∼ 60–66.7 at% H) than γ-hydride (ZrH, FCT, ∼ 50 at% H). Electron energy loos spectroscopy (EELS) measurements prior to APT analyses confirmed the presence of δ-hydride. Hence, APT gives a systematic underestimation of hydrogen for Zr-hydride. Milling at cryogenic temperatures was found to not cause such hydride formation. However, we did not find significant differences in the clusters formed by segregation of the alloying elements Fe, Cr and Ni to irradiation induced a-loops whether the material was identified as α-Zr or hydride. Therefore, analyzing irradiation-induced redistribution of alloying elements in Zr fuel cladding using APT does not rely on FIB preparation at cryogenic temperatures. However, in conjunction with voltage pulsing APT cryo-FIB can be worthwhile if one aims at investigating hydrogen distribution or hydrides.

1. Introduction

Fuel cladding in boiling water nuclear reactors is manufactured from alloyed α-Zr (HCP crystal structure) since Zr has a low thermal neutron capture cross section and Zr-alloys show good corrosion properties. The most relevant degradation mechanisms in the reactor environment are corrosion, hydrogen pick-up (HPU) and irradiation damage. Irradiation by fast neutrons creates vacancies and interstitials, which rearrange and agglomerate, leading to the formation of dislocation loops, which in alloyed Zr can have diameters smaller than 5 nm [1]. These loops lie on certain crystallographic planes [2,3]. Their number, size and type evolve with increasing neutron dose [1,4]. After a short period of irradiation (days to weeks) [1,4] a-loops with Burgers vector $1/3 < 11\bar{2}0 >$ form on close-to prismatic planes and align in layers parallel to the basal plane [2] and reach a saturation density after roughly one year [1]. Later – at the time when significant dimensional changes take place – c-loops with Burgers vector $1/6 > 20\bar{2}3 >$ form [3]. These are purely of vacancy type, lie in the basal plane, and are larger than a-loops in the same material [3].

Zircaloy-2 type alloys are the most widely used as fuel cladding in boiling water reactors (BWRs). Alloying elements are Sn, Fe, Cr, Ni and O. While Sn and O stay in solid solution, nearly the entirety of the transition metals Fe, Cr and Ni – due to their solubility of less than approximately 10 ppm by weight [5] (in agreement with APT data from Zircaloy-4 [6]) – form precipitates that are referred to as secondary phase particles (SPPs). During irradiation, these SPPs are amorphized and dissolve. Fe, Cr and Ni then segregate around dislocation loops [1,7] and form clusters throughout the α-Zr matrix that vary in composition, shape and size [8]. FeCr-clusters are often spheroidal [8,9] while FeNi-clusters are often disk- [8] or ring-shaped [10].

Hydride formation is detrimental to the structural integrity of fuel cladding since ductility is reduced and crack initiation is enhanced [11]. It occurs during operation (as hydrogen is released during Zr oxidation in water) and during cooling (when hydrogen solubility decreases) [11]. The known Zr-hydrides are: ζ-$ZrH_{0.5}$ (FCC, metastable), γ-ZrH (FCT, likely metastable), δ-$ZrH_{1.5-1.7}$ (FCC), and ε-ZrH_2 (FCT) [12]. Of these, δ- and γ-hydride are most often related to mechanical failures [12]. The maximum solubility of hydrogen in Zr is only a few atomic ppm at room temperature

---

[*] Corresponding author.
E-mail addresses: david.mayweg@chalmers.se, david.mayweg@gmail.com (D. Mayweg).

https://doi.org/10.1016/j.jnucmat.2023.154444

[13] and is reported to be largely insensitive to alloying [14–16]. It furthermore does not change significantly with irradiation [17,18]. The terminal solid solubility of hydrogen in Zr around 300 °C (relevant temperature for BWR operation) is approximately 100–150 wt ppm [16]. This fraction is exceeded during operation and eventually leads to the formation of hydrides.

Atom probe tomography (APT) is a powerful microstructural characterization technique that is uniquely capable of reconstructing the 3D position and chemical identity of millions of detected ions from a specimen and has a chemical sensitivity in the in range of a few ppm for all elements [19], and 3D spatial resolution below 1 nm [20]. APT has been used to investigate Zr fuel cladding with respect to irradiation-induced clustering of alloying elements [8,9,21-23], oxidation [24,25], and hydride formation [24,26-28]. Since APT can detect hydrogen, it is the only experimental method capable of characterizing its distributions in materials in 3D on the near-atomic scale [29,30]. However, quantitative hydrogen analysis by APT is challenging since residual hydrogen (gas) is always present in the analysis chamber. The hydrogen from the residual gas cannot be distinguished from the "real" hydrogen originating from the specimen (unless deuterium has intentionally been introduced into the specimens). Additionally, the amount of hydrogen measured can vary significantly depending on measurement conditions [31] and is influenced by specimen preparation [28]. Focused ion beam (FIB) is now the most commonly used specimen preparation technique for APT [32]. This preparation method can induce formation of hydride phases in metals and alloys, most notably Ti [33] and Zr [34,35]. It has been observed e.g. in commercially pure Ti [36] (by APT & transmission electron microscopy (TEM)) and Zircaloy-4 [28] (by APT) [35] (by TEM). When it does not lead to hydride formation it can nevertheless lead to higher hydrogen concentrations (e.g. in Ti6246 [36], Zircaloy-4 [28]). FIB milling at cryogenic temperatures has been shown to suppress hydride formation, likely due to the lowered mobility of hydrogen [28,35,36].

We analyzed a total of 79 Zr data sets from *Zircaloy-2* and *Alloy 2* (a derivative of *Zircaloy-2* with increased Fe and Cr content) in standard (commercial) heat treatment condition as well as α-annealed *Zircaloy-2*. APT specimens were lifted out by FIB at ambient temperature and sharpened by FIB at ambient temperature or under cryogenic conditions, and we additionally analyzed data from earlier studies on electropolished specimens. Unlike most recent APT investigations on Zr [8,9,21-23,26-28,37], we also used voltage instead of laser pulsing to promote the quality and appearance of crystallographic information. These were used to aid in the determination of the captured phases and provide more accurate characterization of clustering.

2. Materials

The compositions of the investigated materials in unirradiated condition given by the manufacturer (Sandvik AB, Sweden) are provided in Table 1. We investigated material from *Zircaloy-2* cladding tubes with heat treatment code *LK3* (*LK* for Swedish '*låg korrosion*', meaning: low corrosion; 3 designates the third iteration in the development of the heat treatment [38], which exhibits an optimized SPP size leading to more uniform corrosion and lower HPU compared to *LK2*) as well as α-annealed *Zircaloy-2* (770 °C) coupons with different cooling rates (details for APT investigations on the latter, see [5]; the material is the same as that investigated in [39]). Additionally, we investigated material from cladding tubes made of *Alloy 2* (heat treatment *LK3*), which is a modification of *Zircaloy-2* (similar to *HiFi*^{TM}) that contains more Fe and Cr to reduce HPU. Cladding tubes (*Zircaloy-2 LK3* and *Alloy 2 LK3*) were analyzed in as-produced, in autoclaved and in irradiated conditions. The irradiated tubes had been exposed to 2082 days of operation in the BWR *Oskarshamn 3*; the coolant saturation temperature was 286 °C (samples from fueled region: fast neutron fluence 24×10^{25} n m^{-2}/ 38 dpa; samples from plenum region: 5.4×10^{25} n m^{-2}/ 8.6 dpa; we used the conversion factor for BWRs from [40] to calculate damage levels from fluences). Average hydrogen concentrations of the cladding tubes post operation were ~ 1.2 at% (*Alloy 2 LK3*) and ~ 1.8 at% (*Zircaloy-2 LK3*) measured by hot vacuum extraction. *Zircaloy-2* coupons were analyzed in unirradiated condition.

3. Experimental

FIB-based specimen preparation on irradiated, as-produced and autoclaved materials was performed using an instrument of type *FEI Versa 3D DualBeam*. Annular milling was conducted at 30 kV with decreasing nominal currents from 1 nA to 50 pA. To remove beam damage and implanted Ga near the surface, final low kV cleaning [41] was performed at 5 kV and 48 pA for approximately 30 s and 2 kV and 28 pA for approximately 120 s. Lamellas for scanning transmission electron microscopy (STEM) were prepared with the same instrument. Some tip specimens were sharpened at −150 ± 2 °C in a *Tescan GAIA3* equipped with a *Leica VCT500* cryo-stage. The cold-finger temperature was approximately − 183 °C. Annular milling was conducted at 30 kV in steps, with currents from 1 nA to 45 pA. Low-kV cleaning was performed at 5 kV with 30 pA for 60 s. After sharpening, the tips were left in the instrument until room temperature was reached (usually overnight) and transferred to the load lock of the APT instrument at ambient conditions in less than five minutes.

The number of collected ions in voltage pulsing APT on cryo-FIB sharpened specimens was significantly lower than that of those sharpened at room temperature. 10 out of 12 cryo-FIBed tips that could be measured fractured between 100,000–600,000 ions, one after approximately 2 million and one after 6 million ions (initial runs were conducted at 70 K, due to very short runs we then used 80 and 90 K). Room-temperature (RT) FIB sharpened tips normally ran for at least a few million ions and up to approximately 15–20 million for the largest data sets. Data sets with less than 300,000 ions or with significant Ga implantation were not included in the hydrogen analysis, leaving 7 cryo-FIBed data sets that were included in the analysis.

Some data from two earlier publications were evaluated, where tips had been prepared by RT-FIB [5] and electropolishing [42]. In the electropolished specimens, no hydride formation was observed. Further information regarding the electropolishing preparation protocol can be found in [42].

Table 1
Chemical compositions (wt%) of the analyzed materials in as-produced condition (provided by the manufacturer, Sandvik AB, Sweden, for *Zircaloy-2 LK3* and *Alloy 2 LK3*; for α-annealed *Zircaloy-2* from [39]).

Alloy designation	Fe	Cr	Ni	Sn	O	C (wt ppm)	Si (wt ppm)
Zircaloy-2 LK3	0.18	0.13	0.061	1.49	0.12	143	91
Alloy 2 LK3	0.36	0.18	0.063	1.31	0.12	120	90
α-annealed Zircaloy-2	0.17	0.11	0.07	1.36	0.13	132	90

Most APT was performed using an *Imago LEAP 3000X HR* (laser wavelength 535 nm), only analyses of tips after prior EELS measurements were performed in a *Cameca LEAP 6000XR* (laser wavelength 266 nm). Voltage mode was used with a pulse repetition rate of 200 kHz, 15 or 20% pulse fraction (PF) and target detection rates of 0.001–0.002 ions/pulse. The latter values are comparatively low and were used to avoid rapid voltage increases that result in earlier fractures. The setpoint temperature was usually 70 K. For a few experiments, we set the temperature to 50 and 60 K for part of a run to obtain clearer crystallographic features and to 80–90 K to achieve longer runs, respectively. The runs on electropolished specimens were conducted between 40 and 130 K. The comparatively high temperatures were used to reduce the risk of specimen fracture during removal of the surface oxide shell stemming from the preparation process. On tips from the region near the oxide-metal interface laser pulsing APT was conducted (mostly laser pulse energy of 0.3–0.4 nJ) since the oxide is non-conductive and cannot be run in voltage pulsing mode. A table of runs including the determined hydrogen fraction and experimental parameters is provided as supplementary material.

We performed ranging for each data set or sub-volume (e.g. to exclude oxides/high O regions) individually. Reconstruction (voxel size 1×1×1 nm, delocalization 3×3×1.5 nm), with crystallographic calibration and elemental quantification were performed in *IVAS 3.6.14*. For high hydrogen voltage runs the time-of-flight correction was performed using the ZrH^{++} peak at 45.5 Da, otherwise the default settings were used. We calculated the image compression factor from indexed poles and k-factor from spatial distribution maps (SDMs) [43]. Based on the Zr^{+++}/Zr^{++} ratio we used a field of 30 V/nm instead of the IVAS default of 28 V/nm [44]. We used AP Suite 6.3 for reconstruction and analysis of the compositions for the experiments performed with the LEAP 6000XR. Peaks included in the hydrogen analysis of voltage pulsing runs were H^+, $H_2{}^+$, ZrH^{+++}, ZrH^+(highlighted in Fig. 2), laser pulsing runs additionally included $Zr_2H_3{}^{+++}$, ZrH^+, $ZrH_2{}^+$, $ZrOH^+$ and $ZrOH_2{}^+$. Peak deconvolution was performed by the built-in function in *IVAS* to solve the overlap between Zr^{++} (Zr^{+++}) and ZrH^{++} (ZrH^{+++}) in spectra from voltage pulsing and additionally ZrH^+ and $ZrH_2{}^{+++}$ in spectra from laser pulsing measurements.

Field evaporation images (FEIs, often called *field desorption maps* or simply *hit maps* in the literature) were created using *MATLAB®* codes ([45] and [46]) and *WinWulff®* [47] was used for stereographic projection overlays. While the ion projections from local electrode atom probes (LEAPs) more closely represent an equidistant-azimuthal projection, the stereographic projection enables an adequate approximation for the purposes of indexing for the angular fields of view captured (< 70°) [48].

STEM and EELS were performed utilizing a transmission electron microscope *FEI Titan 80–300* equipped with a *GIF Tridiem 866* energy filter operated at 300 kV.

4. Results

4.1. Electron microscopy of irradiated fuel cladding

Figure 1(a) shows a backscattered electron (BSE) image of a metal-oxide interface from an irradiated *Alloy 2* sample. The oxide exhibits cracking parallel to the interface, typical for *Zircaloy-2* type cladding [49]. Hydrides are observed inside the metal, mostly in the vicinity of the oxide. Fig. 1(b) shows a STEM micrograph (Z-contrast) of a TEM foil (thickness of approximately 0.8 inelastic mean free paths) from irradiated *Zircaloy-2* prepared by RT-FIB. It originates from a depth of ∼ 2 µm below the metal-oxide interface and is horizontally aligned with it. Regions of low intensity are hydrides. The large hydride (gray dot) with an angle of ca. 30° to the horizontal direction is wider than 100 nm and several µm long. It resembles the morphology of the hydrides seen in Figure 1 (a). Fig. 1(c) shows the plasmon peaks of EELS spectra from the positions indicated by colored dots.

The spectrum from the large hydride (gray) shows a shift of ∼ 2.5 eV with respect to α-Zr (green) and is therefore identified as δ-hydride [50–52]. The purple spectrum in Figure 1 (c) also identifies a δ-hydride, while the red and blue spectra likely correspond to γ-hydride [35] or are caused by an interface effect shifting the δ peak to lower values [53]. It is likely that (all) the smaller hydrides are artifacts from FIB preparation (most likely to occur during final thinning steps to thicknesses < 150 nm), as shown for Zircaloy-4 by Hanlon et al. [35]. The morphology of these small hydrides in Figure 1(b) appears to be similar to that shown in reference [35]. However, there are noteworthy differences between the referenced work and that presented here, i.e., hydrides likely did not form in the same way in the two studies. The cladding material we investigated contains much larger (likely δ- [54]) hydrides before milling (Fig. 1(a) and the one marked with a gray dot in (b)) that formed during operation and/or the (years long) cooling in a spent fuel pool. The strip material investigated by Hanlon et al. was quenched from 400 °C in order to precipitate γ-hydride, which transformed into δ-hydride upon RT-FIB thinning. Since we did not see small hydrides in the initial steps of FIB thinning, we conclude that those are introduced in the final steps. Although only δ-hydride has been reported to form during RT-FIB preparation here EELS has shown that potentially also γ-hydride formation can occur.

4.2. H quantification from APT and EELS measurements

Representative mass-to-charge spectra of two voltage runs are depicted in Fig. 2. Both tips were prepared by Ga-FIB as can be seen from the peaks at 34.5 and 69 Da (representing Ga^{++} and Ga^+ ions, respectively). The spectrum shown in Fig. 2(a) (∼ 7.5×10^6 ions) stems from a tip sharpened at room temperature while the spectrum shown in (b) (∼ 5.2×10^6 ions) stems from a tip where sharpening was conducted at approximately − 150 °C. Hydrogen containing ionic species are highlighted in the plots. In the spectrum from the RT-FIB sharpened tip, H^+-, $H_2{}^+$-, ZrH^{++}- and ZrH^{+++}-peaks of significant magnitude are present. Note that in this specific spectrum, CH^+ was detected as well. This ionic species was however not found in all tips sharpened at room temperature and furthermore is only a small contribution to the overall hydrogen fraction. In the spectrum from the cryo-FIBed tip in (b) hydrogen was only detected as H^+, ZrH^{++} and as CrH^{++} (the latter is unique to this specific spectrum, since the data set contains an FeCr-SPP).

The H^+-peak in (a) is the highest peak in this spectrum and is almost two orders of magnitude higher than the H^+-peak in (b) where the Zr^{3+}-peaks are the highest. The relative field was lower for the specimen in (a) than for that in (b) (Zr^{+++}/Zr^{++} ratios were 1.6 and 21.3, respectively, both constituting a field slightly larger than 30 V/nm [44]). The much lower number of ions collected from the cryo-FIBed tips with low hydrogen fractions might be caused by higher stresses exerted on these tips (Zr has been reported previously not to run well in voltage pulsing APT [55,56]). Fe, Cr and Ni were almost exclusively detected as doubly charged ions avoiding overlaps as typically found in laser pulsing APT (Sn^{++} and Ni^+, ZrC^{++} and Cr^+; ZrO^{++} and Fe^+). In addition, we did not observe a double peak or long tail at 28 Da as often found in laser runs indicating that CO^+ is not present here [42]. Hence, we could confidently assign this peak exclusively to Fe^{++}. Because of the relatively higher electric field environment, a larger fraction of the ions from alloying elements were detected as compared to previously reported laser pulsing measuremenst, where Fe and Cr were only partly detected as doubly charged ions [42] and $CO^+$is present.

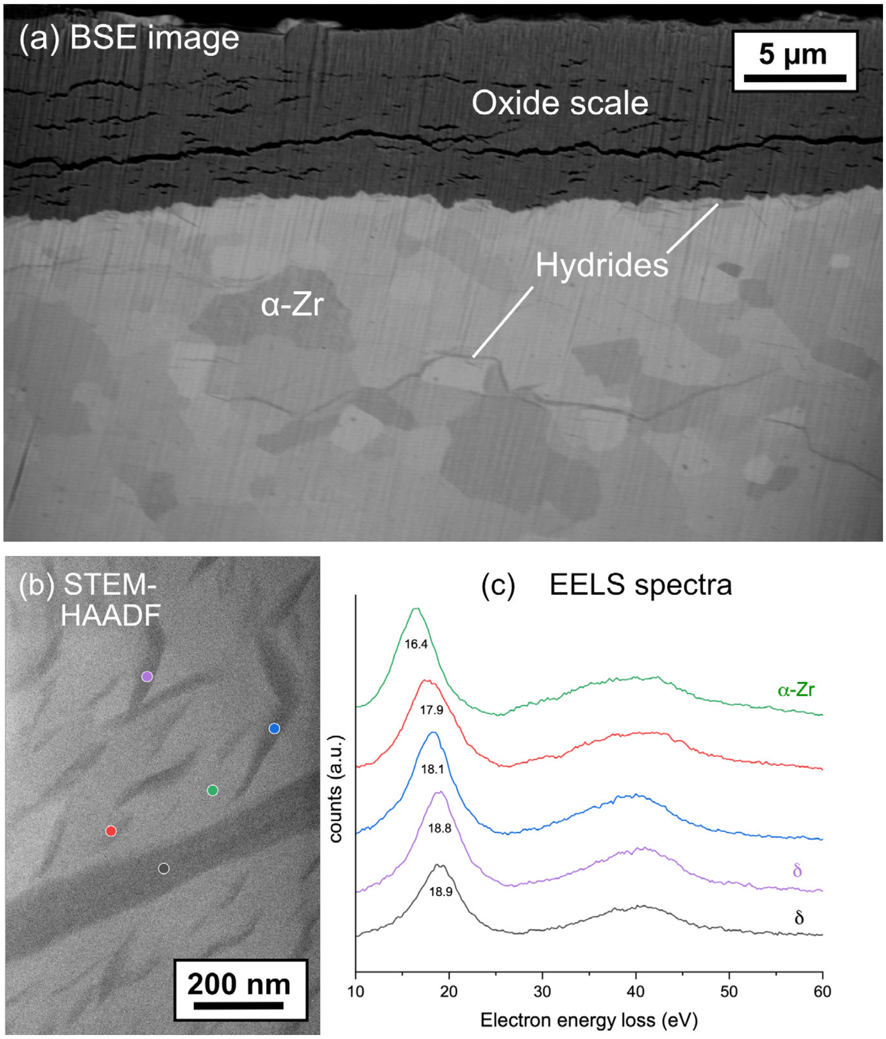

Fig. 1. a) Backscattered electron (BSE) image (31° tilted) of the metal-oxide interface of an *Alloy 2* sample after 2082 days exposure in a BWR. Porosity and cracks are visible in the oxide scale. Both grain boundary and transgranular hydrides are present in the metal. (b) STEM-high angle annular dark field (HAADF) image showing hydrides of different sizes, the formation of the small ones is likely caused by FIB milling. (c) EELS spectra showing plasmon peaks that are representative of α-Zr (green, top) and hydrides (below).

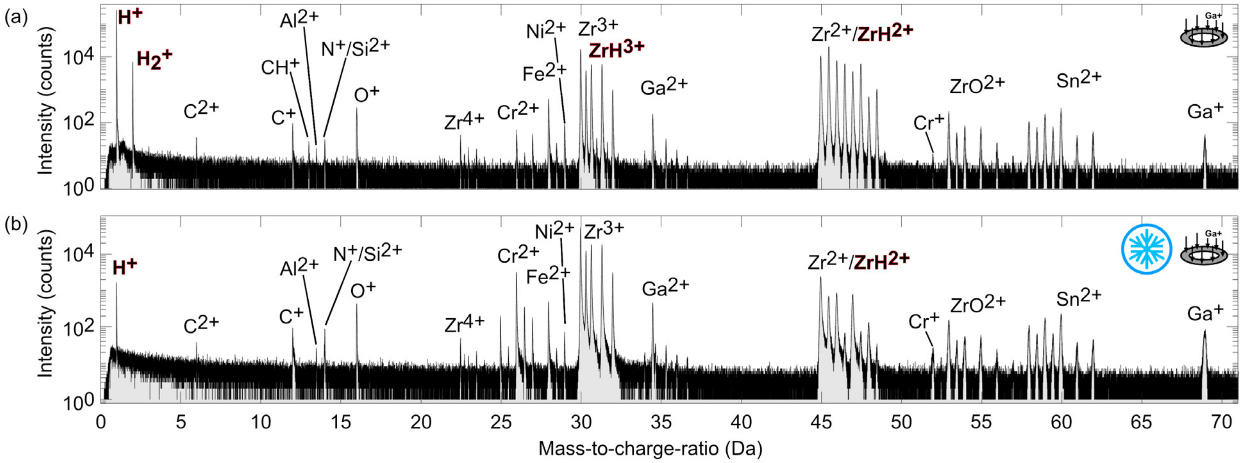

Fig. 2. Mass-to-charge spectra from two APT tips (both irradiated *Alloy 2*) measured in voltage pulsing mode. The spectrum in (a) stems from a tip that was sharpened at room temperature and analyzed at 70 K with a pulse fraction of 20%. The spectrum in (b) stems from a tip that was sharpened at −150 °C and measured at 90 K and pulse fraction of 15%. The ionic species used in the calculation of the hydrogen fraction are marked by red outlines.

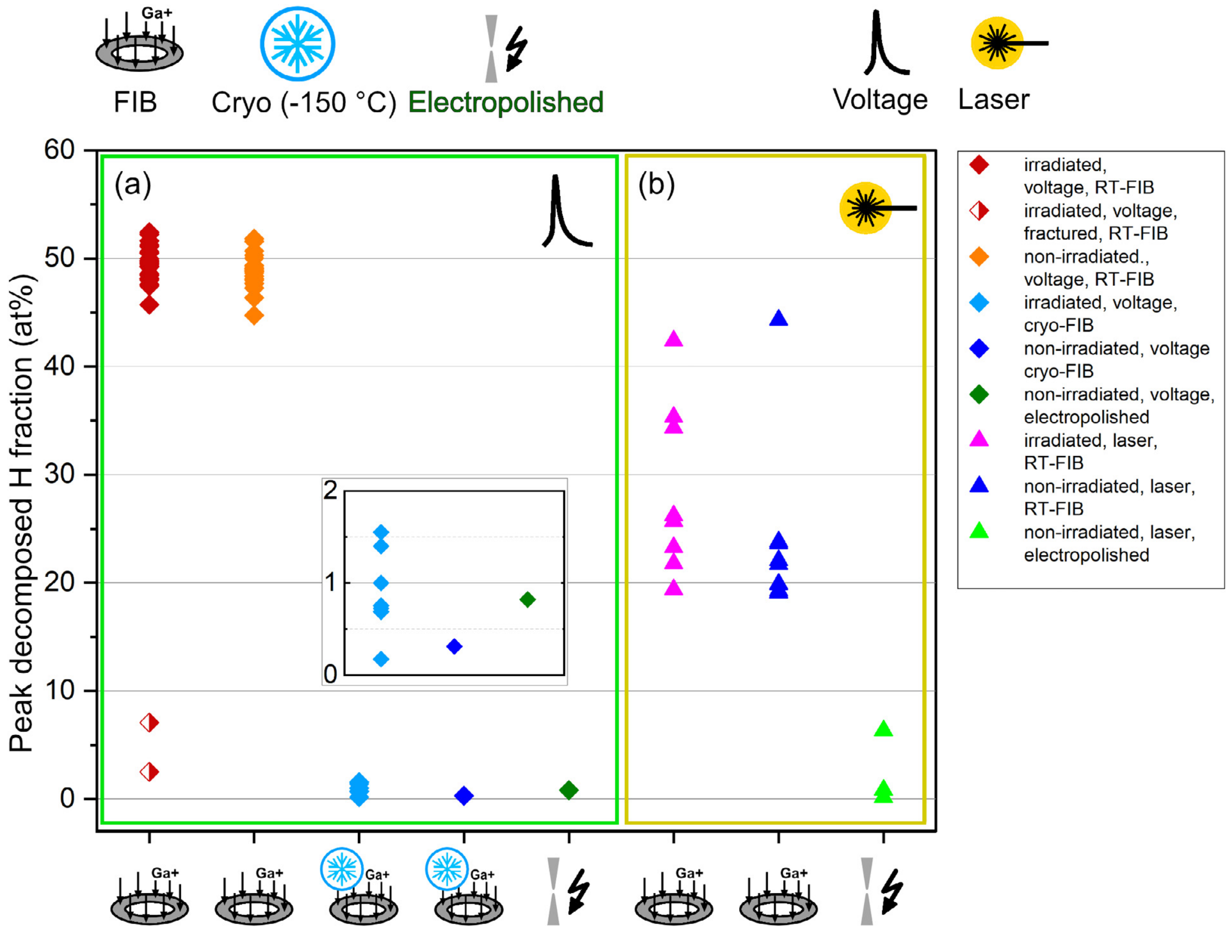

Fig. 3. Hydrogen fractions in Zr fuel cladding materials (*Zircaloy-2* and *Alloy 2* in different conditions) measured by APT. (a) are measurements in voltage and (b) laser mode. Included are irradiated and unirradiated materials prepared by RT- and cryo-FIB (− 150 ± 2 °C) as well as via electropolishing (see symbols at the top). Error bars representing the counting statistics were omitted since they are smaller than the marker dimensions. The inset is an enlarged view of the low hydrogen values measured in voltage pulsing mode.

Figure 3 shows the measured hydrogen fractions from the APT data that we collected. Data sets that contained oxide or SPPs were cropped and only the hydrogen fraction of the Zr matrix was determined. The results are grouped by the different preparation methodologies and material conditions. Preparation methodologies are RT/cryo-FIB sharpening, and electropolishing. Material condition here only refers to irradiated (not differentiated between the 38 and 8.6 dpa materials) and unirradiated material since measured hydrogen fractions were independent of the alloy composition and differences in neutron dose. Icons at the top represent different preparation methodologies and APT modes: (a) voltage and (b) laser measurements. Voltage pulsing APT of RT-FIB sharpened tips (from all materials listed above) contain roughly 50 at% (ranging from ∼ 45–53 at%) hydrogen in the case of irradiated and unirradiated materials alike (red and orange diamonds). Note the two half-filled red diamonds (∼ 7 and ∼ 2.5 at% hydrogen) representing data acquired from measurements that continued after microfractures had occurred. Voltage pulsing of cryo-FIBed tips (irradiated *Alloy 2*, light blue diamonds, and one tip unirradiated *Alloy 2*, dark blue diamond) and electropolished samples (one tip unirradiated *Zircaloy-2*, green diamond) results in measured hydrogen fractions of ∼ 0.2 – 1.5 at% (see inset in Fig. 3). Very low hydrogen fractions of < 0.5 at% were measured in sub-volumes that did not include low index poles and had low amounts of Ga implantation (< ∼ 0.3 at%). Laser pulsing measurements of electropolished tips (light green diamonds) result in hydrogen fractions of ∼ 1 at% hydrogen (one outlier at ∼ 6 at%, likely due to the relatively high temperature of 130 K, which was used in order to "run through" the oxide shell formed during preparation). Laser measurements of RT-FIB milled tips (pink and dark blue triangles) range from ∼ 20–45 at% hydrogen (averaged over each entire data set). Laser measurements of cryo-FIBed specimens were not conducted. Interpretation of measured hydrogen fractions from voltage pulsing measurements shown in Fig. 3 at first glance seems straightforward: RT-FIB sharpened tips contain ∼ 50 at% hydrogen independent of alloy composition and irradiation dose and therefore appear to represent the hydrogen concentration of the material. The measured hydrogen fraction can however be slightly influenced by the experimental parameters used in APT [57] and not all detected hydrogen originates from the specimen. The measured hydrogen fraction depends predominantly on the time between pulses [58]. We varied the pulse frequency (and therefore the time between pulses during which contaminant hydrogen can interact with a tips' surface) in one experiment to study the influence of this parameter on the measured hydrogen fraction: at a pulse frequency of 200 kHz, the hydrogen fraction was measured to be 49.7 at%. A reduction in pulse frequency to 20 kHz led to an increase of the measured hydrogen fraction to 52.3 at%. Linear extrapolation to infinite pulse fraction [58] (i.e., zero time between pulses) results in an estimated hydrogen fraction of 49.4 at%. This means that at the pulse frequency of 200 kHz, which we routinely used, below 1 at% hydrogen is then estimated to originate from other sources (e.g., residual gas molecules in the chamber or humidity picked up during transfer). In addition to the rather small effects that lead to overestimation of hydrogen it has been reported by Chang et al. [31] that significant losses of hydrogen occurred in voltage pulsing of a Ti-hydride. In this specific case it was a deuteride formed in a gaseous deuterium atmosphere ($TiD_{1.92–1.99}$, FCT, approx. 65.8 at%–66.6 at% D) but that observation does not change the fundamental insight with respect to the analysis of hydrogen having a mass of 1 amu. The reported values of the deuterium fraction were 46–50 at% in voltage pulsing, hence there was an underestimation of 15–20 at% with respect to the expected stoichiometry. Several potential causes for loss of hydrogen (D) are mentioned by Chang et al. [31]: first, delayed co-evaporation of hydrogen containing (molecular) ions; second, ions evaporating sometime after the pulse and third, potential formation of neutral ions by dissociation of molecular ions. From the assessment of ion correlation histograms [59] we found some evidence of co-evaporation of ion pairs or delayed evaporation as shown by Chang et al. [31]. However, it was less severe than in the referenced work and it is not clear if this provides a sufficient explanation for a comparable loss of hydrogen (compare the plot in [31] and Figure S4 in the supplementary material).

It is noteworthy that we saw a much lower fraction of multiples measured in our LEAP 3000X HR (35–42% multiple hits; detection efficiency 37%) although the nominal hydrogen concentration in the deuteride from Chang et al. and the here presented δ-hydride is quite similar (approximately 66–67 at%). In the newer generation LEAPs used by Chang et al. the number of multiples were reported to be 60%–65% for the instrument with a reflectron (LEAP 5000XR: detection efficiency 50%) and 70%–75%, respectively for the straight flight-path instrument (LEAP 5000XS: detection efficiency 80%). It is unclear if this observation is related to the instrument or to a more general difference in the field evaporation behavior of Ti- and Zr-hydrides (for example TiH_2 molecular ions are mostly observed in analyses of Ti-hydrides, while for Zr it is mostly ZrH) possibly in combination with differing experimental parameters that do not allow for a direct comparison. However, for the quantification of hydrogen fractions the difference in detected multiple event seems not to be relevant since the underestimation of hydrogen is similar for all instruments.

To overcome this ambiguity with respect to the actual hydrogen fraction we performed EELS measurements on tips prior to APT experiments. The result from the only successful measurement where voltage and laser pulsing were performed on the same specimen after EELS measurements is presented in Fig. 4.

Figure 4(a) depicts a HAADF STEM image (stitched from two micrographs since the inhomogeneous thickness makes the adjustment of brightness and contrast challenging) of an APT tip of irradiated *Alloy 2*, sharpened by RT-FIB milling. The regions from which EELS spectra were collected are marked by the numbered rectangles. The plasmon peaks of the EELS spectra from the positions in Fig. 4(a) are shown in (b) in the same colors. As expected, the number of counts becomes lower with increasing specimen thickness, which is noted as mean free path (MFP) above the rectangles in Fig. 4(a). The main peak in spectrum 1 is at approximately 19.3 eV, while a “shoulder” indicating a further peak is located at approximately 16.9 eV. These positions correspond to δ-hydride and α-Zr, respectively [52]. Spectrum 2 and 3 with their (local) maxima at 17.0 eV exhibit shoulders around 19.2 eV, while the maximum of spectrum 4 is located at 17.0 eV. The depicted spectra provide conclusive evidence for the presence of a δ-hydride [52], which is most clear for the thinnest regions of the specimen. Going down the shank the transformation seems to be only partial as can be concluded from the presence of peaks characteristic of δ-hydride and α-Zr in spectrum 2 and 3.

The APT measurements conducted after recording of the EELS spectra only captured a small volume close to the apex. This tip was run in voltage mode (70 K, pulse fraction 15%, only approx. 140,000 ions were collected since the success rate of voltage pulsing measurement after TEM-imaging was very low) and then in laser mode (1.5×10^6 ions, 70 K, 50 pJ, 266 nm laser wavelength). Hydrogen quantification resulted in approximately 46 at% and 28 at% for voltage and laser pulsing mode, respectively. EELS spectra from three further tips showed the presence of δ-hydride at or near the apex. Of these tips two were measured in laser pulsing APT (one tip was lost during transfer and two had SPPs near or at the apex, one can be found in the supplementary material, see Figure S1).

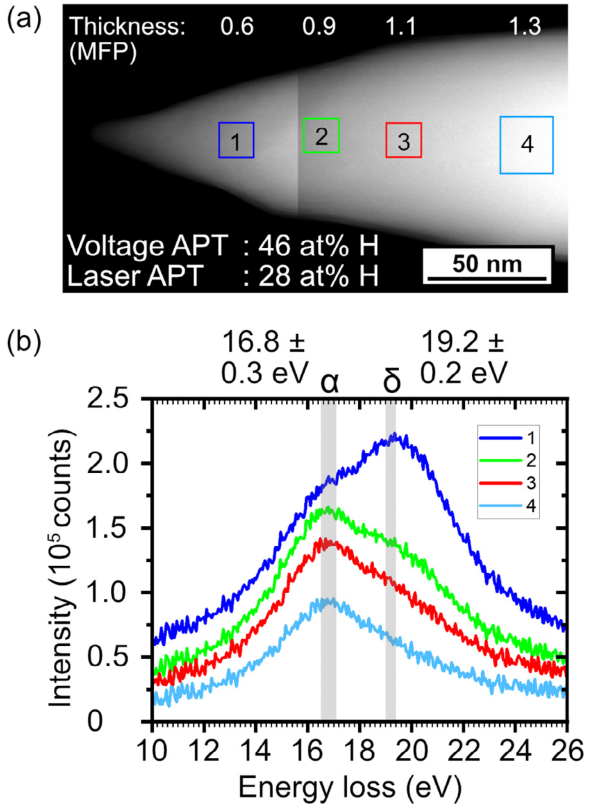

Fig. 4. EELS measurements on a tip (irradiated *Alloy 2*, 8.6 dpa) prepared by RT-FIB. (a) is a HAADF STEM image of an APT tip, coloured rectangles show regions where the STEM-EELS spectra were recorded, the thickness (as mean free path) is indicated at the top. (b) EELS spectra from the positions in (a).

The results presented in Fig. 4 make it very unlikely that the measured hydrogen fractions close to 50 at% from voltage pulsing APT (Fig. 3), which is close to that expected in γ-hydride [13], are representing the materials’ actual composition. The EELS spectra instead show the presence of δ-hydride that has a higher hydrogen fraction. This observation agrees with the work from Hanlon et al. [35] as explained in Section 4.1. As mentioned in detail above, the deviation of the measured hydrogen fraction from the expected hydride stoichiometry in APT has previously been shown by Chang et al. [31]. When considering our own observations presented above together with the insights from the literature, it is most likely that our APT data also represent a significant underestimation of hydrogen of approximately (15–20 at%) and that RT-FIB induces the formation of δ-hydride in APT tips from Zr.

We did not find a significant difference between irradiated and unirradiated cladding (red and orange diamonds in Fig. 3(a)). The two half-filled red diamonds in Fig. 3(a) (run continued after specimen microfracture) support the notion that FIB-induced hydrides are only present within a few hundred nm from the tips’ apexes as was evident from the EELS analysis in Fig. 4.

Final sharpening by FIB conducted at cryogenic temperatures eliminated the largest portion of hydrogen as was discussed for the spectra depicted in Fig. 2 and so did electropolishing. However, even the lowest measured hydrogen fractions of ~ 0.2–0.5 at% (that roughly agree with the estimated fraction of hydrogen not origination from the sample in a δ-hydride tip as described above) still significantly exceed the solubility of hydrogen in *Zircaloy-2* (~ 1 wt ppm [17] at room temperature) and, for comparison, are also higher than the amount of hydrogen found by APT in steels where we often measure ~ 0.1 at% in voltage pulsing. Whatever the reason for the still significant amount of hydrogen – whether it originates from within the specimens or the analysis chamber– the fraction is far lower than in known Zr hydrides, leading us to conclude that the measured volumes with low hydrogen fractions are most likely α-Zr.

Results from laser pulsing APT measurements (Figure 3(b)) have much larger scatter as the measured hydrogen fraction depends more strongly on the analysis conditions (especially laser pulse energy) [31] and, in addition, the hydrogen distribution within the volumes is inhomogeneous as has been shown for Zr-hydrides in [26,28] and Ti-deuterides [31]. Visual assessment by isoconcentration surfaces shows that the local concentration ranges approximately 20–80 at% with the high concentration volumes being on the side opposite from where the laser illuminates the specimens (see supplementary material Figure S1). These inhomogeneities are likely caused by surface diffusion and inhomogeneous evaporation and therefore laser pulsing is not recommended when attempting hydrogen analysis [31]. However, despite the large scatter in laser pulsing measurements (which makes analyses targeting hydrogen practically impossible), like voltage runs they show that RT-FIB sharpening leads to high hydrogen fractions. As the specimens analyzed in laser mode were prepared in the same manner as the RT-FIBed specimens analyzed in voltage mode, it is reasonable to assume that these specimens are of the same phase, particularly when coupled with the evidence from EELS data in Fig. 4.

4.3. APT crystallography

APT data sometimes contains valuable crystallographic information that can aid the analysis; crystallographic features are most clearly visible in voltage pulsing. Fig. 5 depicts FEIs from voltage pulsing APT on unirradiated (a), (b) and irradiated specimens (c), (d) that were sharpened by different methods: (a) and (b) by RT-FIB, (c) by cryo-FIB milling, and (d) by electropolishing. Measured hydrogen fractions are noted above the FEIs. All FEIs show density variations due to local magnification effects, i.e., altered ion trajectories caused by electric field differences across terraced specimen surfaces. Regions of high-density variation correspond to crystallographic features. The FEIs in Fig. 5(a) and (b) show three- and four-fold symmetry both of which are not found in HCP structures. FEIs are overlain with stereographic projections from δ-hydride (a), (b) and α-Zr (c), (d). The supplementary material (see Figure S2 and S3 with further details) also provides overlays with the stereographic projections of γ-hydride, which we initially assumed to be more likely to be present based on the hydrogen quantification resulting in ~ 50 at%.

Additionally, interplanar spacings along different poles were measured during crystallographic calibration of the data sets (using a section of the voltage curves with approximately 2,000,000 ions) shown in (b) and (c). These interplanar spacings listed in Table 2 and show a good agreement between theoretical (calculated from lattice parameters given in [12]) and measured values.

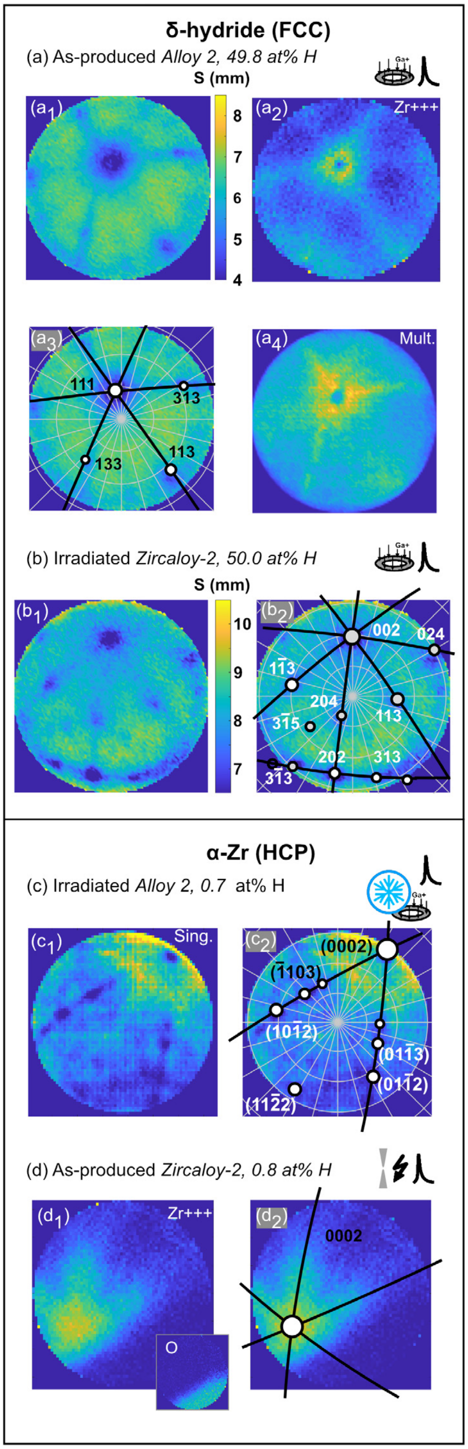

Fig. 5. Field evaporation images (FEIs) from voltage measurements on Zr fuel cladding materials from (a), (b) RT-FIB, (c) cryo-FIB sharpened and (d) electropolished tips. (a) and (b) are δ-hydride (FCC); (c) and (d) are α-Zr (HCP). Stereographic projections of the respective phase are overlain onto the FEIs. Great and small circles on the Wulff nets are marked in steps of 15° and 10° respectively, in (d) they are omitted since only one pole is visible and so the field of view cannot be determined.

The FEIs from specimens with significant hydrogen fraction and pole and zone line symmetries not found in HCP α-Zr add to the evidence that they correspond to hydride phases. Fig. 5(a_1) shows an FEI of the average distance (in mm, symbol *S*) between consecutive hits on the detector (created with the MATLAB code from [46]) for a RT-FIBed specimen (unirradiated *Alloy 2)* with a measured hydrogen fraction of 50 at%. At first sight the zone-line symmetry around the dominant pole could be mistaken to be six-fold. Plotting specific ionic species (Zr^{+++}-ions in Fig. 5(a_2) and multiple events in (a_4)) however, shows three-fold symmetry characteristic

Table 2
Comparison of the values of interplanar spacings measured from spatial distribution maps (SDMs) and those calculated from the crystal structures of δ-hydride and α-Zr for several poles in Fig. 5.

Pole	Interplanar spacing, theoretical (pm)	Interplanar spacing from SDMs (pm)	Deviation (%)
Fig. 3(b) δ-hydride			
(002)	239.0	240	< +1
(202)	169.0	159	+ 6
(204)	106.9	115	+ 8
(024)	106.9	105	– 2
(113)	144.1	149	– 6
Fig. 3(c) α-Zr			
(0002)*	257.5	238	– 8
$(0\bar{1}12)$	189.5	191	+ 1
$(0\bar{1}13)$	146.3	151	+ 3
$(\bar{1}103)$	146.3	154	+ 5
$(11\bar{2}2)$	136.8	128	– 6

* This SDM might be influenced by distortion of trajectories near the edge of the data set.

for a {111} pole in an FCC (or potentially near three-fold for FCT) crystal structure. In the overlay with the stereographic projection depicted in Fig. 5(a$_3$) of δ-hydride, the poles and zone line positions fit well (slightly better than γ-hydride, see supplementary material). Fig. 5(b) is another example from RT-FIBed material (irradiated *Zircaloy-2*) with a measured hydrogen fraction of 50 at%. It exhibits a different crystallographic orientation than shown in (a) as can be seen in the Zr^{++}-FEI in (b$_1$). This image clearly reveals the positions of multiple poles and zone lines and the overlain stereographic projection in (b$_2$) with the fourfold (002) pole corresponding to δ-hydride fits very well (see Table 2), as do the ratios between the interplanar spacings of major poles that were calculated from SDMs [60]. The evidence based on hydrogen fraction and the crystallographic pattern shown in the FEI again confirm that the phase captured is δ-hydride.

The FEI depicted in Fig. 5(c$_1$) shows the density of single ion detection events across the detector space from an irradiated *Alloy 2* specimen sharpened at cryogenic temperature (– 151 °C). The measured hydrogen fraction in the APT dataset was comparatively low (0.7 at%). Zone lines and poles are visible and the overlay with the stereographic projection in (c$_2$) of α-Zr fits well. Additionally, the measured interplanar spacings agree well with the expected values of α-Zr (see Table 2). We conclude therefore that the phase captured is α-Zr. Fig. 5(d) depicts an FEI from an electropolished specimen (unirradiated *Zircaloy-2)*, also with low measured hydrogen fraction (0.8 at%). This FEI (d$_1$) was created using only Zr^{+++} ions. An SDM at the center of the high-density region revealed periodicity of the ion count in this direction, thus representing a pole position; the zone lines are characteristic of a six-fold (0002) pole. The low Zr^{+++}/high O region at the lower left (compare with small inset, where O containing ions are plotted) has a high O fraction of ~ 30 at%. This is an artifact from the electropolishing process that creates a shell of oxide (and O saturated α-Zr) at the surface of the tip. This compositional difference partially obscures the zone lines. The stereographic overlay of HCP α-Zr on the Zr^{+++}-FEI fits well, however, and in combination with the chemical composition confirms that the measured volume is likely α-Zr. Note that in Fig. 5(c) and (d) a clear difference in the appearance of the (0002) poles in the α-Zr FEIs can be observed. We attribute this to the fact that the experiments were conducted at different temperatures [61] ((c) at approximately 90 K and (d) at approximately 130 K).

Small deviations in the pole and zone line positions compared to the stereographic projection overlays can also be observed, e.g., in Fig. 5(c$_2$). An equidistant-azimuthal projection model [48] might have provided a more accurate fit to the crystal patterns observed in the FEIs but there is a lack of software currently available to do this. Development of software to do an equidistant-azimuthal overlay falls outside the scope of the presented study. However, the stereographic projection overlays used here provide an approximate fit to sufficiently index the crystallographic identity of poles and zone lines. Small deviations also observed in the measured plane spacings compared to the nominal plane spacings shown in Table 2 can be attributed to simplifying assumptions used in the tomographic reconstruction algorithm. After crystallographically calibrating the reconstructions [62], deviations of the measured plane spacings from the theoretical values are expected, as previously reported in studies such as [63,64].

5. Discussion

Recent APT studies of Zr have mostly used laser pulsing and including hydrogen in the analyses has largely been omitted [5,8-10,21,22,65,66]. Studies in which it was analyzed – with respect to deuterides (i.e., hydrides grown after artificial introduction of deuterium into the material) in Zircaloy-4 [26,28] – showed some ambiguity with respect to the hydride phases, the measured hydrogen (or deuterium) fractions and the influence of FIB-sharpening. That is, in some cases large hydrogen (or deuterium) fractions, indicating a phase transformation into a hydride, were found while in other cases such a behavior was not observed. In addition, the crystallographic features that were present, were not sufficiently clear to distinguish between FCC (δ-hydride) and FCT (γ- and ε-hydride) [28]. In the here presented investigations, we employed voltage APT to improve data quality, especially with respect to the crystallographic information [67], to be able to confidently determine the hydride phase by analyzing APT data. Since there was ambiguity with respect to the measured hydrogen composition, we conducted correlative APT and EELS measurements that provided evidence for the presence of δ-hydride. Hence, APT is indeed underestimating the hydrogen fraction as reported e.g. by Chang et al. [31]. An advantage of voltage pulsing is that the measured hydrogen fraction is relatively consistent between specimens compared to laser pulsing. In addition, the reduced number of molecular ions and overlapping peaks allow for more reliable analysis of the composition. As mentioned above, in the present case this especially concerns hydrogen (to a lesser extent Fe, Cr and Ni). One disadvantage of using voltage pulsing in comparison to laser pulsing is the smaller the size of data sets that usually is obtained since the higher voltage leads to earlier specimen fracture.

5.1. α-Zr → hydride transformation

We have provided evidence that – for *Zircaloy-2* type materials – RT-FIB sharpening leads to a transformation from α-Zr into δ-hydride. In assessing the presented results combining EELS and crystallographic features in the FEIs we showed that although measured chemical composition deviates significantly from the actual composition, δ-hydride can be identified with high confidence. Cryo-FIB sharpening and electropolishing do not cause such a transformation. This is in good agreement with the behavior of *Zircaloy-4* [28] and Ti-alloys [36]. The here investigated materials however seem to be even more prone to a FIB-induced formation of hydrides. Unlike *Zircaloy-4* and Ti where the α-phase is often present after RT-FIB prep [36,68,69] we saw δ-hydride formation in *every* APT tip when sharpened at room temperature irrespective of the hydrogen concentration of the bulk material. The direct formation of stable δ-hydride in bulk material depends mainly on the cooling rate [70]. It forms at comparatively slower cooling rates compared to γ-hydride, which subsequently can transform into δ [71,72]. For sub-µm sized material, such as TEM foils and APT tips, internal stresses slowing down such a process likely do not play a role and might allow for a fast formation of δ-hydride. As cited above there exists evidence that γ-hydrides in thin TEM foils transform into δ-hydrides during RT-FIB milling [35] and recently nano-sized hydrides with a δ-hydride core and γ-hydride rim were reported [53]. The formation mechanism of δ-hydrides observed in our work might therefore occur via an initial α-Zr $\rightarrow$ γ-hydride transformation as proposed by Carpenter [73]. This transformation is realized by shear on alternating basal planes and hydrogen atoms taking tetrahedral sites [13]. The magnitude of shear caused by Shockley partials of type $1/3 < 10\bar{1}0 >$ is approximately 0.1 nm and the transformation goes along with a volume increase of 12.3% [74] compared to pure α-Zr. The transformation relies on hydrogen diffusion, which in the present case likely is facilitated through the energy inputted by the ion beam [36]. The final $\gamma \rightarrow \delta$ transformation then, which is associated with a total volume increase (compared to α-Zr) of 17.2% [74], is then expected to occur via compression along the c-axis and an expansion along the a-axes of the γ-hydride.

5.2. Comparison of clusters in α-Zr and δ-hydride

Irradiation-induced clustering of mainly Fe, Cr and Ni in *Zircaloy-2* fuel cladding occurs when these alloying elements (initially are located in $Zr_2(Fe,Ni)$- and $Zr(Fe,Cr)_2$-SPPs) are redistributed inside the material and segregate to dislocation loops.

Since Cr diffuses much slower than Fe and Ni [75], the distribution of Cr throughout the material is more inhomogeneous [5] and therefore Cr concentrations are highest close to dissolving SPPs. In general, the cluster appearance is expected to vary strongly depending on the SPP composition, the received dose, the temperature and most importantly with the distance to SPPs [76]. Due to the fact that hydrogen has been excluded from most prior clustering analyses of APT data [8-10,22,77] the question arises whether the observed FIB-induced hydride formation is relevant for analyzing irradiation-induced clustering in such alloys. The phases of the reconstructions displayed in Fig. 6 were identified by the presented methods to determine the hydrogen fraction and the crystallographic features: α-Zr in Fig. 6(a) and δ-hydride in Figure 6 (b), both from *Alloy 2* (38 dpa). The FEI in Fig. 6(c) shows the characteristic six-fold (0002) pole from HCP α-Zr associated with a hydrogen fraction of $\sim$ 1.0 at% in the Zr matrix. The FEI in Fig. 6(d) indicates the presence of δ-hydride similar to Fig. 5(a) and which is supported by the measured hydrogen fraction of 49.8 at%. Both tips exhibit clustering of Fe, Cr and Ni (pink, blue and green, respectively) at what are assumed to be a-loops. Clusters are aligned in parallel layers, which are depicted with an edge-on view. Layers have a mean distance of 16±4 nm in the α-Zr (a) and 19±4 nm (b) in the δ-hydride (calculated from 1D concentration profiles in the [0002] and a $\langle 111 \rangle$ direction, i.e., the layer spacing is slightly larger in the δ-hydride. The position of the (0002) pole in (c) is approximately 30° off the center of the FEI in (c). This is in good agreement with the inclination of the layers and confirms that clusters are aligned parallel to basal planes. Due to the transformation into δ-hydride, layers in the tip shown in Figure 6 (b) are now parallel to one set of {111} planes, instead of (0002) planes which is consistent with an orientation relationship often observed between α-Zr and δ-hydride [70].

Although there are clearly visible differences in the appearance of the clusters with respect to size, shape, composition and number this is explained (at least in part) by the presence of the SPP visible in the α-Zr volume. Clusters near the SPP have the highest Cr fraction, while almost no Cr is present after about 100 nm distance, which can be explained by the lower diffusivity of Cr compared to Fe [75]. Cr is less evenly distributed than Fe and Ni in the δ-hydride volume, too, being mostly located near the apex of the reconstructed volume. The clearly visible difference in cluster composition (FeCr- vs. FeNi-cluster) is in accordance with previous observations [1,9,22]. Due to the compositional differences, that are found throughout most, if not all, APT measurements of irradiation-induced clustering in *Zircaloy-2* type fuel cladding [9] a direct comparison of (few) APT data sets or individual layers or clusters can only yield insights that leave some uncertainty since clustering shows great variability even within individual data sets.

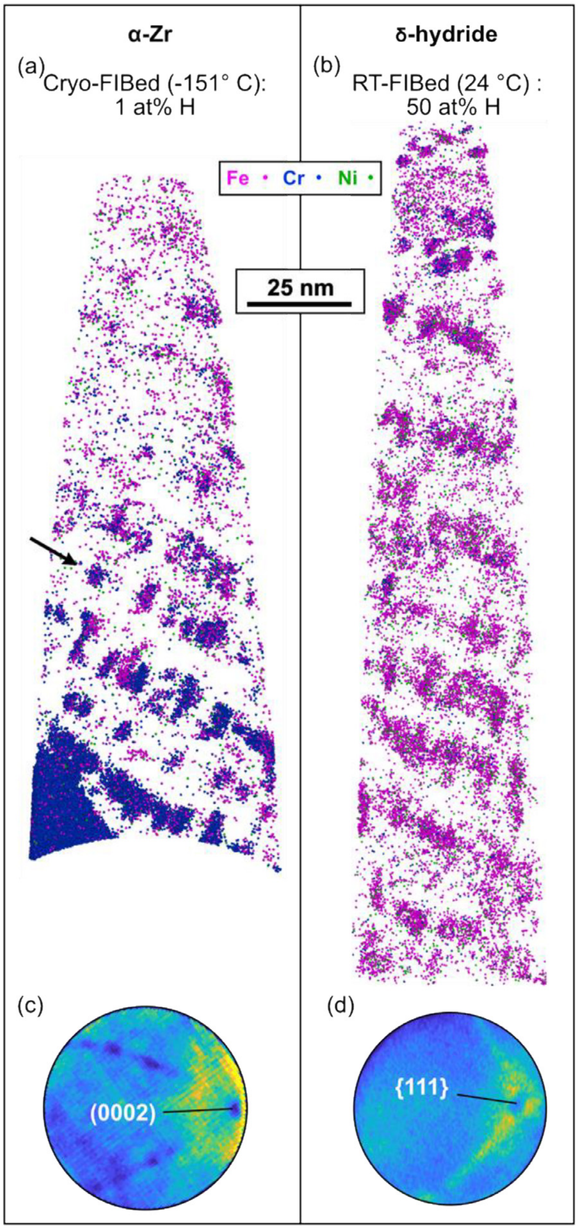

Fig. 6. Reconstructions from APT measurements on irradiated *Alloy 2* fuel cladding (38 dpa). (a) α-Zr (cryo-FIB preparation, 15 nm slice) and (b) δ-hydride (RT-FIB). Both exhibit clustering of Fe, Cr and Ni (colored pink, blue and green, respectively) at $<a>$-loops, which are aligned in layers on average spaced 14 and 19 nm apart. They are parallel to the (former) basal planes. The depiction shows the layers edge-on. FEIs the α-Zr (0002) pole in (c) and a δ-hydride {111} pole in (d). In the α-Zr an SPP was partially captured as can be seen on the lower left in (a). The layer marked by the black arrow in (a) is analyzed in more detail later in this section.

In the data set depicted in Figure 6 (b) we found a small volume exhibiting a low hydrogen fraction (< 1 at%), meaning that it is not transformed into hydride. This volume is displayed in Fig. 7(a) and (c). The low-hydrogen region is clearly visible in (a) where all hydrogen containing ions are displayed in dark yellow. It is furthermore highlighted in (c) by a 4.5 at% hydrogen ICS. Hydrogen declines from about 48 at% to below 1 at% (top); at the

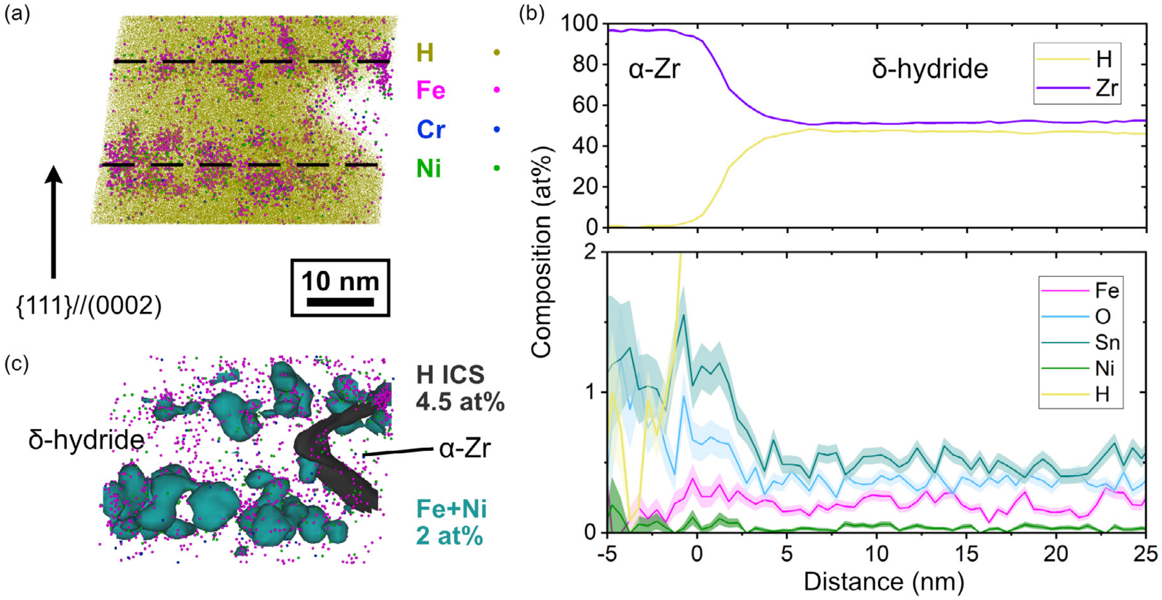

Fig. 7. Two layers of clusters in a hydrided data set where a small region was not transformed, (a) depicts all detected hydrogen-containing ions as well as Fe, Cr and Ni, (b) uses ICSs to highlight clusters and the low hydrogen region (black). (c) shows proxigrams of the hydrogen ICS shown in (c).

same time the O and Sn fractions (these elements remain mostly in solid solution) roughly double (bottom graph). What is additionally noteworthy with respect to the transformation is that no rejection of Sn can be observed, as was seen for hydride growth in [26]. This speaks for a displacive transformation with hydrogen as the only mobile species. The clusters that extend from the hydride into the Zr region seem not to be affected. The decrease in Fe that is observed in the proxigram is caused by the fact that the α-Zr "wedge" in Fig. 7 is located in-between the two layers of clusters, which contain the transition metal alloying elements.

To provide some measure of comparison we took an attempt at quantitatively analyzing layers with similar visual appearance. Fig. 8 depicts examples of clustering within one well-defined individual layer from (a) α-Zr (*Alloy 2,* 38 dpa) and one from (b) FIB-induced δ-hydride (*Zircaloy-2,* 38 dpa). Although stemming from these two different alloys, we believe that this comparison makes sense, which we expound upon in this section.

The layer shown in Fig. 8(a) stems from the cryo-FIB sharpened data set shown in Fig. 6(a) (marked by a black arrow), which has the highest Cr fraction of all data sets that we investigated (~ 0.41 at%, excluding the SPP, hydrogen excluded). The layer in Fig. 8(b) stems from the data set with the highest Cr fraction (~ 0.16 at%, with hydrogen excluded from the analysis) that we measured in voltage mode on RT-FIB sharpened tips (out of almost 30 voltage run data sets from irradiated *Alloy 2* and *Zircaloy-2*). Clusters in both layers exhibit similar spheroidal shapes as has been reported previously for Cr-rich clusters from laser pulsing atom probe [8–10]. The Fe:Cr ratio in the layer shown in Fig. 8(a) is roughly 1:1 while it is approximately 1:3 in the layer depicted in Fig. 8(b). As explained above, these ratios are on the high Cr side and represent only a small difference compared to the scatter in the Fe:Cr ratio of clusters found in reactor irradiated *Zircaloy-2* fuel cladding of different fluences [9]. The layers depicted in Fig. 8 are viewed along the [0002] (a) and <111> direction (b). Fig. 8(a_1) and (b_1) display all Fe, Cr and Ni ions detected inside the volumes (thickness 12 nm). The images in (a_2) and (b_2) additionally depict Fe+Cr+Ni isoconcentration surface (ICSs), which show qualitative similarity. Note that the equivalent of the 4 at% ICSs in α-Zr (a_2) are 2 at% ICSs for these elements in δ-hydride (b_2) since roughly 50 at% hydrogen was added by FIB preparation in the latter. (a_3) and (b_3) depict 24 and 23 clusters, respectively, which were extracted based on the ICSs depicted in (a_2) and (b_2). The result from cluster analysis using the maximum separation method [78] (parameters: $N_{min} = 10$; $d_{max} = 0.65$ nm, which was chosen since for both layers analyzed it was a local minimum in a number density vs. d_{max} parameter sweep [79] with step size 0.05 nm; and $L = d_{erosion} = 0.45$ nm) are displayed in Fig. 8(a_4) and (b_4). Based on this cluster identification, 28 clusters were detected in each of the layers and Fe and Cr fractions of 11 and 18 at% for the clusters in α-Zr and 38 and 15 at% for those in δ-hydride (with hydrogen excluded from the composition) were found. Note that these values deviate from the values given above for the volume incorporating the whole layer due to the uneven distribution within the volumes.

Figure 9 shows the results from the quantitative cluster analysis of the clusters visually presented in Fig. 8(a_4) and (b_4) by a plotting the ratio (Fe+ Cr+Ni)/Zr over the number of total ions per cluster. Hydrogen was excluded from this analysis. It exhibits a similar distribution for both analyzed volumes and confirms the qualitative similarity that was found by visual inspection as shown above.

The volume increase that is associated with the observed transformation in our view does not affect the general approach to cluster analysis, since their number density, composition, size and shape of clusters scatter significantly more within individual specimens or within individual grains (Fig. 6 and e.g. [5,8-10,21,22]). The same is valid for the atomic displacements due to the transformation, which is approximately 0.1 nm for Zr positions. Assuming this is the magnitude that the solute atoms located in clusters are displaced by as well, this will likely not be noticeable due to limitations of the spatial resolution in APT, which is especially degraded in clusters [20].

Previous APT studies on this matter, where δ-hydride specimens have been analyzed, are thus still valid. It might even be beneficial to analyze the δ-hydride phase, since the number of collected ions is much larger for hydrided specimens (even excluding the collected hydrogen ions making up about half on the total number) due to the relative ease with which field evaporation can

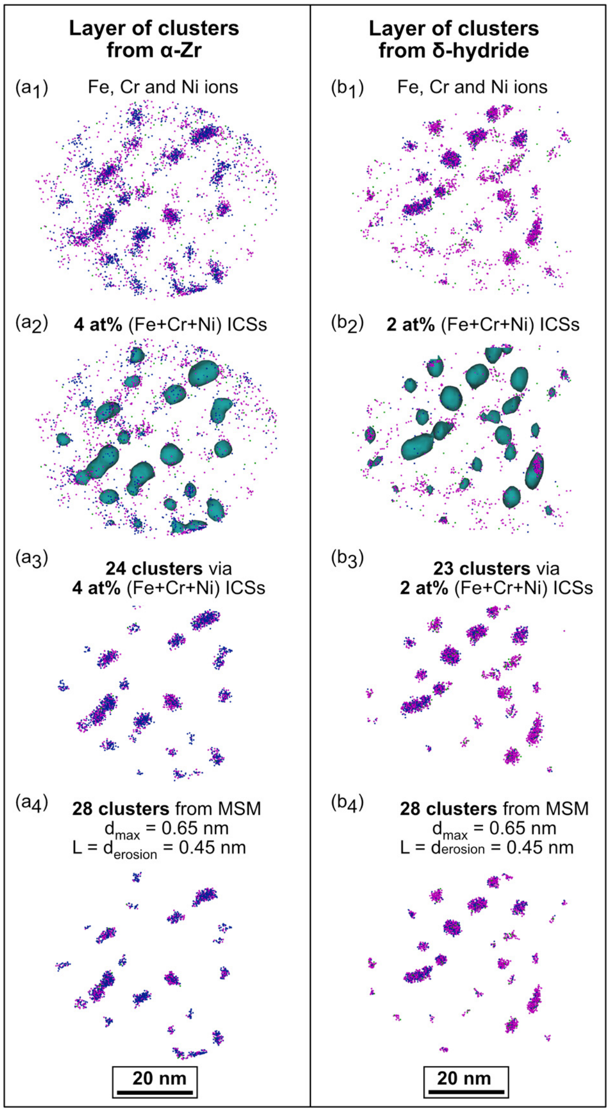

Fig. 8. Comparison of clusters of Fe (pink), Cr (blue) and Ni (green) in (a) α-Zr and (b) δ-hydride. The images at the top depict all Fe, Cr and Ni ions from one individual layer of α-Zr and δ-hydride with views on the (0002) and a {111} plane, respectively. Both volumes extend 12 nm into the image plane. Clusters contain mostly Fe and Cr. The images in (a_2) and (b_2) show Fe+Cr+Ni ICSs as indicated. (a_3) and (b_3) depict the volumes extracted via these ICSs and (a_4) and (b_4) are the visual representation of the results from cluster analysis using the maximum separation method.

be triggered as compared to α-Zr tips. This likely includes alloys other than those of *Zircaloy-2* type like *Zircaloy-4* and Zr-Nb alloys although both show a lesser tendency to exhibit hydrides after RT-FIB [28].

Since the fraction of measured hydrogen in cryo-FIBed tips was in some cases clearly below 1 at% (similar to the bulk content of the irradiated material, in which, however, most hydrogen is located in hydrides), such an experimental procedure might enable improved hydrogen analyses, e.g., confirming hydrogen trapping sites. Preparation at cryogenic temperatures is furthermore helpful if hydrides that are present in, e.g., autoclaved or irradiated (*Zircaloy-2* type) fuel cladding before FIB milling are targeted to be analyzed by APT. Recent advances with hydrogen charging, cryogenic preparation and transfer under cryogenic conditions [80] should also be exploited in future work.

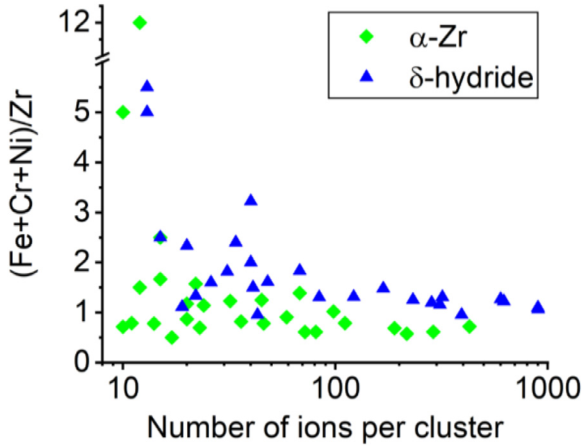

Fig. 9. Quantitative description of clustering for the layers shown in Fig. 8. The plot shows the ratios of the sum of solute (Fe, Cr and Ni) ions to Zr ions over the total number of ions per cluster.

6. Conclusions

In summary, we conclude our investigations as follows:

- The compositional information gathered from voltage APT (approx. 50 at% hydrogen, close to the composition of γ-hydride) is not sufficient to identify the correct FIB-induced hydride phase in the here investigated Zr materials.
- The APT data deviate from the actual composition, as evidenced by EELS measurements, which proved the presence of δ-hydride ($\sim$ 60–66,7 at% hydrogen) based on the plasmon peak position.
- Careful assessment of the crystallographic information (FEIs and interplanar spacings) contained in APT data then revealed a closer agreement with δ-hydride rather than γ-hydride.
- The hydrogen-fraction of the tips sharpened at cryogenic temperature of approximately −150 °C was close to or even below 1 at%. These tips' crystallography was in excellent agreement with α-Zr.
- We did not find that the α-Zr to δ-hydride transformation induced by the ion beam at room temperature has an observable effect on cluster size, shape or composition. Therefore, APT analyses that are undertaken to characterize clustering do not rely on sample preparation at cryogenic temperatures.
- For APT analysis targeting hydrogen, including hydrides, it is necessary to employ FIB sharpening at cryogenic temperature. It is furthermore advised to use voltage pulsing, in contrast to laser pulsing, since the measured hydrogen fraction is more consistent. Employing such measures might open an opportunity to gain further insight into the hydrogen related degradation mechanisms of Zr alloys at operation in nuclear reactors that have been inaccessible to direct observation in the past.

Supplementary material

Further information on the hydrogen distribution in laser pulsing APT, crystallographic analysis and hydrogen loss as well as a table of conducted APT runs (represented by the data points in Figure 3) are available in the supplementary material.

Declaration of Competing Interest

The authors declare that they have no known competing financial interests or personal relationships that could have appeared to influence the work reported in this paper.

CRediT authorship contribution statement

David Mayweg: Conceptualization, Validation, Formal analysis, Investigation, Writing – original draft, Writing – review & editing, Visualization. **Johan Eriksson:** Investigation, Writing – original draft, Writing – review & editing. **Olof Bäcke:** Investigation, Writing – review & editing. **Andrew J. Breen:** Formal analysis, Writing – review & editing. **Mattias Thuvander:** Conceptualization, Supervision, Writing – original draft, Project administration, Funding acquisition.

Data availability

The APT data sets are part of ongoing investigations. POS/EPOS files may be shared upon reasonable request from DM or MT.

Acknowledgements

This work was carried out at Chalmers Materials Analysis Laboratory (CMAL). DM is thankful for funding from Svenskt Kärntekniskt Centrum/the Swedish Centre for Nuclear Technology (SKC). JE an MT acknowledge financial support from Westinghouse, Vattenfall, OKG and EPRI. AJB acknowledges funding through the Australian Department of Industry, Innovation and Science under the auspices of the AUSMURI program and the scientific and technical assistance of the Microscopy Australia node at the University of Sydney (Sydney Microscopy & Microanalysis). We thank Baptiste Gault for helpful comments on assessing the Field of View in the LEAP instruments used in this work. Hans-Olof Andrén and Gustav Sundell are acknowledged for fruitful discussions regarding hydrogen quantification by APT. And, we are thankful to Pia Tejland and Magnus Limbäck for providing fuel cladding samples and to the MIDAS and MUZIC-3 communities for collaboration.

Supplementary materials

Supplementary material associated with this article can be found, in the online version, at doi:10.1016/j.jnucmat.2023.154444.

References

[1] A. Harte, D. Jädernäs, M. Topping, P. Frankel, C.P. Race, J. Romero, L. Hallstadius, E.C. Darby, M. Preuss, The effect of matrix chemistry on dislocation evolution in an irradiated Zr alloy, Acta Mater. 130 (2017) 69–82.
[2] A. Jostsons, P.M. Kelly, R.G. Blake, The nature of dislocation loops in neutron irradiated zirconium, J. Nucl. Mater. 66 (3) (1977) 236–256.
[3] M. Griffiths, A review of microstructure evolution in zirconium alloys during irradiation, J. Nucl. Mater. 159 (1988) 190–218.
[4] G.J.C. Carpenter, D.O. Northwood, The contribution of dislocation loops to radiation growth and creep of Zircaloy-2, J. Nucl. Mater. 56 (1975) 260–266.
[5] J. Eriksson, D. Mayweg, G. Sundell, H.-.O. Andrén, M. Thuvander, Solute concentrations in the matrix of zirconium alloys studied by atom probe tomography, ASTM STP 1645 (2022).
[6] N. Ni, D. Hudson, J. Wei, P. Wang, S. Lozano-Perez, G.D.W. Smith, J.M. Sykes, S.S. Yardley, K.L. Moore, S. Lyon, R. Cottis, M. Preuss, C.R.M. Grovenor, How the crystallography and nanoscale chemistry of the metal/oxide interface develops during the aqueous oxidation of zirconium cladding alloys, Acta Mater. 60 (20) (2012) 7132–7149.
[7] E. Bettini, T. Eriksson, M. Boström, C. Leygraf, J. Pan, Influence of metal carbides on dissolution behavior of biomedical CoCrMo alloy: SEM, TEM and AFM studies, Electrochim. Acta 56 (25) (2011) 9413–9419.
[8] J. Eriksson, G. Sundell, P. Tejland, H.-.O. Andrén, M. Thuvander, An atom probe tomography study of the chemistry of radiation-induced dislocation loops in Zircaloy-2 exposed to boiling water reactor operation, J. Nucl. Mater. 550 (2021) 152923.
[9] J. Eriksson, G. Sundell, P. Tejland, H.-.O. Andrén, M. Thuvander, Nanoscale chemistry of Zircaloy-2 exposed to three and nine annual cycles of boiling water reactor operation — an atom probe tomography study, J. Nucl. Mater. 561 (2022) 153537.
[10] T. Sawabe, T. Sonoda, An atom probe study on the Fe distribution in Zr-based alloys with different Fe content under high fluence neutron irradiation, J. Nucl. Mater. 567 (2022) 153809.
[11] A.T. Motta, L. Capolungo, L.-.Q. Chen, M.N. Cinbiz, M.R. Daymond, D.A. Koss, E. Lacroix, G. Pastore, P.-C.A. Simon, M.R. Tonks, B.D. Wirth, M.A. Zikry, Hydrogen in zirconium alloys: a review, J. Nucl. Mater. 518 (2019) 440–460.
[12] J. Bair, M. Asle Zaeem, M. Tonks, A review on hydride precipitation in zirconium alloys, J. Nucl. Mater. 466 (2015) 12–20.
[13] E. Zuzek, J.P. Abriata, A. San-Martin, F.D. Manchester, The H-Zr (hydrogen-zirconium) system, Bull. Alloy Phase Diagram. 11 (4) (1990) 385–395.
[14] J.J. Kearns, Terminal solubility and partitioning of hydrogen in the alpha phase of zirconium, Zircaloy-2 and Zircaloy-4, J. Nucl. Mater. 22 (3) (1967) 292–303.
[15] A. Sawatzky, B.J.S. Wilkins, Hydrogen solubility in zirconium alloys determined by thermal diffusion, J. Nucl. Mater. 22 (3) (1967) 304–310.
[16] K. Une, S. Ishimoto, Dissolution and precipitation behavior of hydrides in Zircaloy-2 and high Fe Zircaloy, J. Nucl. Mater. 322 (1) (2003) 66–72.
[17] K. Une, S. Ishimoto, Y. Etoh, K. Ito, K. Ogata, T. Baba, K. Kamimura, Y. Kobayashi, The terminal solid solubility of hydrogen in irradiated Zircaloy-2 and microscopic modeling of hydride behavior, J. Nucl. Mater. 389 (1) (2009) 127–136.
[18] K. Une, S. Ishimoto, Terminal solid solubility of hydrogen in unalloyed zirconium by differential scanning calorimetry, J. Nucl. Sci. Technol. 41 (9) (2004) 949–952.
[19] P.H. Clifton, T.J. Gribb, S.S.A. Gerstl, R.U. Ulfig, D.J. Larson, Performance advantages of a modern, ultra-high mass resolution atom probe, Microsc. Microanal.: Off. J. Microsc. Soc. Am. Microbeam Anal. Soc. Microscop. Soc. Canada 14 (2008) 454–455.
[20] F. De Geuser, B. Gault, Metrology of small particles and solute clusters by atom probe tomography, Acta Mater. 188 (2020) 406–415.
[21] G. Sundell, M. Thuvander, P. Tejland, M. Dahlbäck, L. Hallstadius, H.O. Andrén, Redistribution of alloying elements in Zircaloy-2 after in-reactor exposure, J. Nucl. Mater. 454 (1–3) (2014) 178–185.
[22] T. Sawabe, T. Sonoda, Evolution of nanoscopic iron clusters in irradiated zirconium alloys with different iron contents, J. Nucl. Sci. Technol. 55 (10) (2018) 1110–1118.
[23] B.M. Jenkins, J. Haley, M.P. Moody, J.M. Hyde, C.R.M. Grovenor, APT and TEM study of behaviour of alloying elements in neutron-irradiated zirconium-based alloys, Scr. Mater. 208 (2022) 114323.
[24] D. Hudson, A. Cerezo, G.D.W. Smith, Zirconium oxidation on the atomic scale, Ultramicroscopy (2009) 667–671.
[25] Y. Dong, A.T. Motta, E.A. Marquis, Atom probe tomography study of alloying element distributions in Zr alloys and their oxides, J. Nucl. Mater. 442 (1–3) (2013) 270–281.
[26] A.J. Breen, I. Mouton, W. Lu, S. Wang, A. Szczepaniak, P. Kontis, L.T. Stephenson, Y. Chang, A.K. da Silva, C.H. Liebscher, D. Raabe, T.B. Britton, M. Herbig, B. Gault, Atomic scale analysis of grain boundary deuteride growth front in Zircaloy-4, Scr .Mater. 156 (2018) 42–46.
[27] I. Mouton, A.J. Breen, S. Wang, Y. Chang, A. Szczepaniak, P. Kontis, L.T. Stephenson, D. Raabe, M. Herbig, T.B. Britton, B. Gault, Quantification challenges for atom probe tomography of hydrogen and deuterium in Zircaloy-4, Microsc. Microanal. 25 (2) (2019) 481–488.
[28] I. Mouton, Y. Chang, P. Chakraborty, S. Wang, L.T. Stephenson, T. Ben Britton, B. Gault, Hydride growth mechanism in zircaloy-4: investigation of the partitioning of alloying elements, Materialia 15 (2021) 101006.
[29] J. Takahashi, K. Kawakami, Y. Kobayashi, T. Tarui, The first direct observation of hydrogen trapping sites in TiC precipitation-hardening steel through atom probe tomography, Scr. Mater. 63 (2010) 261–264.
[30] J. Takahashi, K. Kawakami, Y. Kobayashi, Origin of hydrogen trapping site in vanadium carbide precipitation strengthening steel, Acta Mater. 153 (2018) 193–204.
[31] Y.H. Chang, I. Mouton, L. Stephenson, M. Ashton, G.K. Zhang, A. Szczpaniak, W.J. Lu, D. Ponge, D. Raabe, B. Gault, Quantification of solute deuterium in titanium deuteride by atom probe tomography with both laser pulsing and high-voltage pulsing: influence of the surface electric field, New J. Phys. 21 (5) (2019) 053025.
[32] T.J. Prosa, D.J. Larson, Modern focused-ion-beam-based site-specific specimen preparation for atom probe tomography, Microsc. Microanal. 23 (2) (2017) 194–209.
[33] R. Ding, I.P. Jones, In situ hydride formation in titanium during focused ion milling, J. Electron. Microsc. (Tokyo) 60 (1) (2011) 1–9.
[34] H.H. Shen, X.T. Zu, B. Chen, C.Q. Huang, K. Sun, Direct observation of hydrogenation and dehydrogenation of a zirconium alloy, J. Alloys Compd. 659 (2016) 23–30.
[35] S.M. Hanlon, S.Y. Persaud, F. Long, A. Korinek, M.R. Daymond, A solution to FIB induced artefact hydrides in Zr alloys, J. Nucl. Mater. 515 (2019) 122–134.
[36] Y. Chang, W. Lu, J. Guenole, L.T. Stephenson, A. Szczpaniak, P. Kontis, A.K. Ackerman, F.F. Dear, I. Mouton, X. Zhong, S. Zhang, D. Dye, C.H. Liebscher, D. Ponge, S. Korte-Kerzel, D. Raabe, B. Gault, Ti and its alloys as examples of cryogenic focused ion beam milling of environmentally-sensitive materials, Nat. Commun. 10 (1) (2019) 942.
[37] M.E. Jones, A.J. London, A.J. Breen, P.D. Styman, S. Sikotra, M.P. Moody, D. Haley, Improving the quantification of deuterium in zirconium alloy atom probe tomography data using existing analysis methods, Microsc. Microanal. 28 (4) (2021) 1245–1254.
[38] J. Romero, L. Hallstadius, M. Owaki, G. Pan, K. Kataoka, K. Kakiuchi, R.J. Comstock, J. Partezana, A. Mueller, M. Dahlbäck, A. Garde, A. Atwood, M. Åslund, Evolution of westinghouse fuel cladding, Proceedings of WRFPM/TopFuel, Sendai, Japan, 2014.

[39] B. Hutchinson, B. Lehtinen, M. Limbäck, M. Dahlbäck, A study of the structure and chemistry in Zircaloy-2 and the resulting oxide after high temperature corrosion, ASTM STP 1505 (2007) 269–284.
[40] L. Walters, S.R. Douglas, M. Griffiths, Equivalent radiation damage in zirconium irradiated in various reactors, ASTM STP 1597 (2018) 676–690.
[41] K. Thompson, D. Lawrence, D.J. Larson, J.D. Olson, T.F. Kelly, B. Gorman, In situ site-specific specimen preparation for atom probe tomography, Ultramicroscopy 107 (2–3) (2007) 131–139.
[42] M. Thuvander, H.-O. Andrén, Methods of quantitative matrix analysis of Zircaloy-2, Ultramicroscopy 111 (6) (2011) 711–714.
[43] B. Gault, M.P. Moody, F. de Geuser, G. Tsafnat, A. La Fontaine, L.T. Stephenson, D. Haley, S.P. Ringer, Advances in the calibration of atom probe tomographic reconstruction, J. Appl. Phys. 105 (3) (2009).
[44] D.R. Kingham, The post-ionization of field evaporated ions: a theoretical explanation of multiple charge states, Stem. Cells Int. 116 (2) (1982) 273–301.
[45] P. Felfer, Atom probe toolbox, https://github.com/peterfelfer/Atom-Probe-Toolbox, (accessed November 22nd 2021)
[46] A.J. Breen, A.C. Day, B. Lim, W.J. Davids, S.P. Ringer, Revealing latent pole and zone line information in atom probe detector maps using crystallographically correlated metrics, Ultramicroscopy 243 (2023) 113640.
[47] S. Weber, https://www.jcrystal.com/products/winwulff/. (accessed January 28th 2022).
[48] F. De Geuser, B. Gault, Reflections on the projection of ions in atom probe tomography, Microsc. Microanal. 23 (2) (2017) 238–246.
[49] P. Tejland, H.-O. Andrén, Origin and effect of lateral cracks in oxide scales formed on zirconium alloys, J. Nucl. Mater. 430 (1–3) (2012) 64–71.
[50] H. Zhao, J.-P. Morniroli, A. Legris, A. Ambard, Y. Khin, L. Legras, M. Blat-Yrieix, Identification and characterization of a new zirconium hydride, J. Microsc. 232 (2008) 410–421.
[51] H. Zhao, M. Blat-Yrieix, J.-P. Morniroli, A. Legris, L. Thuinet, Y. Khin, A. Ambard, L. Legras, Characterization of zirconium hydrides and phase field approach to a mesoscopic-scale modeling of their precipitation, ASTM STP 1505 (2008) 29–48.
[52] O.T. Woo, G.J.C. Carpenter, Identification of zirconium hydrides by electron energy loss spectroscopy, Scr. Metall. 20 (3) (1986) 423–426.
[53] N.N. Badr, F. Long, Y. Lou, M. Topping, L.K. Béland, Z. Yao, M.R. Daymond, On the trigonal structure of the ζ-hydride in zirconium: a microstructural characterization approach by electron diffraction and energy-loss spectroscopy, Acta Mater. 247 (2023) 118729.
[54] R.S. Daum, Y.S. Chu, A.T. Motta, Identification and quantification of hydride phases in Zircaloy-4 cladding using synchrotron X-ray diffraction, J. Nucl. Mater. 392 (3) (2009) 453–463.
[55] B. Wadman, U. Rolander, H.O. Andrén, Matrix composition of ZIRCALOY-4, J. de Physique Colloque 48 (C6) (1987) C6–299-C6-304.
[56] B. Wadman, H.-O. Andrén, U. Rolander, Preferential field evaporation during atom probe analysis of ZIRCALOY-4, J. de Physique Colloque 49 (C6) (1988) C6–323 -C6-32.
[57] G. Sundell, M. Thuvander, H.-O. Andrén, Hydrogen analysis in APT: methods to control adsorption and dissociation of H2, Ultramicroscopy 132 (2013) 285–289.
[58] M.S. Meier, M.E. Jones, P.J. Felfer, M.P. Moody, D. Haley, Extending estimating hydrogen content in atom probe tomography experiments where H2 molecule formation occurs, Microsc. Microanal. 28 (4) (2021) 1231–1244.
[59] D.W. Saxey, Correlated ion analysis and the interpretation of atom probe mass spectra, Ultramicroscopy 111 (6) (2011) 473–479.
[60] B.P. Geiser, T.F. Kelly, D.J. Larson, J. Schneir, J.P. Roberts, Spatial distribution maps for atom probe tomography, Microsc. Microanal. 13 (6) (2007) 437–447.
[61] B. Gault, M.P. Moody, J.M. Cairney, S.P. Ringer, Atom Probe Microscopy, Springer, New York, 2012.
[62] B. Gault, D. Haley, F. de Geuser, M.P. Moody, E.A. Marquis, D.J. Larson, B.P. Geiser, Advances in the reconstruction of atom probe tomography data, Ultramicroscopy 111 (6) (2011) 448–457.
[63] A.C. Day, A.J. Breen, S.P. Ringer, A Crystallography-Mediated Reconstruction (CMR) approach for atom probe tomography: solution for a singleton pole, Ultramicroscopy 224 (2021) 113262.
[64] M.P. Moody, B. Gault, L.T. Stephenson, D. Haley, S.P. Ringer, Qualification of the tomographic reconstruction in atom probe by advanced spatial distribution map techniques, Ultramicroscopy 109 (7) (2009) 815–824.
[65] G. Sundell, M. Thuvander, H.-O. Andrén, Enrichment of Fe and Ni at metal and oxide grain boundaries in corroded Zircaloy-2, Corros. Sci. 65 (2012) 10–12.
[66] T. Sawabe, T. Sonoda, S. Kitajima, T. Kameyama, Analysis of atomic distribution in as-fabricated Zircaloy-2 claddings by atom probe tomography under high--energy pulsed laser, J. Nucl. Mater. 442 (1–3) (2013) 168–174.
[67] B. Gault, M.P. Moody, J.M. Cairney, S.P. Ringer, Atom probe crystallography, Mater. Today 15 (9) (2012) 378–386.
[68] F.F. Dear, P. Kontis, B. Gault, J. Ilavsky, D. Rugg, D. Dye, Mechanisms of Ti3Al precipitation in hcp α-Ti, Acta Mater. 212 (2021) 116811.
[69] B.V. Cockeram, P.D. Edmondson, K.J. Leonard, B.F. Kammenzind, J.L. Hollenbeck, Atom probe examinations of Zircaloy irradiated at nominally 358°C, Nucl. Mater. Energy 19 (2019) 416–432.
[70] J.S. Bradbrook, G.W. Lorimer, N. Ridley, The precipitation of zirconium hydride in zirconium and zircaloy-2, J. Nucl. Mater. 42 (2) (1972) 142–160.
[71] B. Nath, G.W. Lorimer, N. Ridley, The relationship between gamma and delta hydrides in zirconium-hydrogen alloys of low hydrogen concentration, J. Nucl. Mater. 49 (3) (1974) 262–280.
[72] B. Nath, G.W. Lorimer, N. Ridley, Effect of hydrogen concentration and cooling rate on hydride precipitation in α-zirconium, J. Nucl. Mater. 58 (2) (1975) 153–162.
[73] G.J.C. Carpenter, The precipitation of γ-zirconium hydride in zirconium, Acta Metall. 26 (8) (1978) 1225–1235.
[74] G.J.C. Carpenter, The dilatational misfit of zirconium hydrides precipitated in zirconium, J. Nucl. Mater. 48 (3) (1973) 264–266.
[75] R.A. Perez, H. Nakajima, F. Dyment, Diffusion in alpha-Ti and Zr, Mater. Trans. 44 (1) (2003) 2–13.
[76] A. Harte, M. Topping, P. Frankel, D. Jädernäs, J. Romero, L. Hallstadius, E.C. Darby, M. Preuss, Nano-scale chemical evolution in a proton-and neutron-irradiated Zr alloy, J. Nucl. Mater. 487 (2017) 30–42.
[77] G. Sundell, Atomic scale degradation of zirconium alloys for nuclear applications, 2015.
[78] J.M. Hyde, C.A. English, An analysis of the structure of irradiation induced Cu-enriched clusters in low and high nickel welds, MRS Online Proc. Lib. 650 (1) (2001) R6.6.
[79] R.P. Kolli, D.N. Seidman, Comparison of compositional and morphological atom-probe tomography analyses for a multicomponent Fe-Cu steel, Microsc. Microanal. 13 (4) (2007) 272–284.
[80] H. Khanchandani, L.T. Stephenson, D. Raabe, S. Zaefferer, B. Gault, Hydrogen/Deuterium charging methods for the investigation of site-specific microstructural features by atom probe tomography, Microsc. Microanal. 28 (S1) (2022) 1664.